

Article

Conceptual Design of a Novel Autonomous Water Sampling Wing-in-Ground-Effect (WIGE) UAV and Trajectory Tracking Performance Optimization for Obstacle Avoidance

Yüksel Eraslan 

Aerospace Engineering Department, Faculty of Aeronautics and Astronautics, Tarsus University, Mersin 33400, Türkiye; yukseleraslan@tarsus.edu.tr

Abstract: As a fundamental part of water management, water sampling treatments have recently been integrated into unmanned aerial vehicle (UAV) technologies and offer eco-friendly, cost-effective, and time-saving solutions while reducing the necessity for qualified staff. However, the majority of applications have been conducted with rotary-wing configurations, which lack range and sampling capacity (i.e., payload), leading scientists to search for alternative designs or special configurations to enable more comprehensive water assessments. Hence, in this paper, the conceptual design of a novel long-range and high-capacity WIGE UAV capable of autonomous water sampling is presented in detail. The design process included a vortex lattice solver for aerodynamic investigations, while analytical and empirical methods were used for weight and dimensional estimations. Since the mission involved operation inside maritime traffic, potential obstacle avoidance scenarios were discussed in terms of operational safety, and the aim was for autonomous trajectory tracking performance to be improved by means of a stochastic optimization algorithm. For this purpose, an artificial intelligence-integrated concurrent engineering approach was applied for autonomous control system design and flight altitude determination, simultaneously. During the optimization, the stability and control derivatives of the constituted longitudinal and lateral aircraft dynamic models were predicted via a trained artificial neural network (ANN). The optimization results exhibited an aerodynamic performance enhancement of 3.92%, and a remarkable improvement in trajectory tracking performance for both the fly-over and maneuver obstacle avoidance modes, by 89.9% and 19.66%, respectively.

Keywords: water sampling; wing-in-ground-effect UAV; conceptual design; obstacle avoidance; trajectory tracking performance; optimization



Citation: Eraslan, Y. Conceptual Design of a Novel Autonomous Water Sampling Wing-in-Ground-Effect (WIGE) UAV and Trajectory Tracking Performance Optimization for Obstacle Avoidance. *Drones* **2024**, *8*, 780. <https://doi.org/10.3390/drones8120780>

Academic Editor: Abdessattar Abdelkefi

Received: 11 November 2024

Revised: 9 December 2024

Accepted: 17 December 2024

Published: 21 December 2024



Copyright: © 2024 by the author. Licensee MDPI, Basel, Switzerland. This article is an open access article distributed under the terms and conditions of the Creative Commons Attribution (CC BY) license (<https://creativecommons.org/licenses/by/4.0/>).

1. Introduction

Water is a vital resource for the survival of ecosystems and humanity. However, in the contemporary era, access to clean water is currently facing considerable challenges due to the contamination of water, driven by a multitude of factors, such as agricultural, chemical, industrial, or mining waste [1,2]. Therefore, the implementation of effective water management approaches and an investigation into the underlying causes of water pollution are crucial issues in ensuring the continuous availability of clean water.

Water sampling treatments serve as an essential tool in water management by means of water quality assessment, pollution detection, trend analysis, ecosystem monitoring, or resource management. Applications vary, depending on the objective of the sampling, such as surface water sampling, depth profiling, composite sampling, groundwater sampling, time-integrated sampling, or sediment sampling. The assessment of water samples is traditionally carried out using separate laboratory analyses following their collection, whereas modern in situ sampling enables collection and real-time measurement simultaneously, but this application is expensive and requires more complex equipment and sensors on the sampling device [3]. In any one of these applications, the location of the sampling (i.e.,

oceans, seas, rivers, lakes, coastal areas, or groundwater) entails the selection of appropriate vehicles and equipment.

The increasing demand for precise and inexpensive sampling has prompted interest in using unmanned aerial vehicles, especially drones, with their advantages in terms of reduced operational costs, a reduced necessity for qualified staff, reduced human-based risk, improved access to difficult areas due to their small size, and an improved ability to gather high-precision data in a shorter time than boats [4,5], sampling stations [6,7], or submersibles [8,9]. Accordingly, over the past few decades, a number of studies have been presented on the design and testing of UAVs and their relevant components for water sampling purposes. For instance, Manoharan et al. [10] developed, prototyped, and tested an autonomous amphibious coaxial quadrotor UAV for water-based applications. Flight tests of the vehicle with a maximum payload of 15 kg showed that the endurance of the vehicle reached 8 min, which resulted in a very limited range at a flight speed of 5 m/s. Sanim et al. [11] redesigned a rotary-wing UAV system that provided non-destructive multi-point sample collection with a 750 mL (3×250 mL) capacity and endurance up to 45 min. Ore et al. [12] proposed a novel water sampling mechanism mounted on an autonomous hexa-rotor UAV with a 600 g payload capacity and 20 min endurance that was capable of capturing a 60 mL (3×20 mL) sample from multiple stations per mission. The purpose of the design was to succeed in tasks requiring small amounts of samples, such as limnology, environmental monitoring, or disease tracking. Moreover, Koparan et al. [13] studied a novel adaptive water sampling device to be used on UAVs for in situ water quality evaluations. This literature review shows that studies have mainly focused on autonomous operations, since current state-of-the-art applications have evolved to be automatic and remotely available. Furthermore, most of the studies were found to be focused on the design and application of sampling apparatuses mounted on pre-existing aerial vehicles [14–18]. Consequently, the majority of these limited design attempts have focused on rotary-wing configurations and, consequently, have constraints in terms of range and/or sampling capacity (i.e., payload).

In water sampling, the amount of water to be collected is based on the type of analysis, which is determined by authority organizations such as the United States Environmental Protection Agency (EPA), the American Public Health Association (APHA), and the International Organization for Standardization (ISO). While the detection of biological contamination or chlorophyll-a, microcystin, and other cyanotoxins requires the collection of at least 1 L of water, the detection of polycyclic aromatic hydrocarbons (PAHs) and special microbiological analyses require 2 L and 5 L of water samples, respectively. The need for such a large amount of water samples, combined with the demand for long ranges, is very challenging to achieve using most existing rotary-wing UAV applications. In order to overcome such constraints, fixed-wing configurations could provide a proper alternative, with their higher cruise speeds, extended ranges, and higher payload capacities.

The range and payload capacity of a fixed-wing aircraft rely on the propulsive, aerodynamic, and structural performance of the vehicle. Since water sampling operations require flight over water surfaces, a wing-in-ground-effect (WIGE) aircraft could be an advantageous candidate, due to its superiority in terms of aerodynamic performance and corresponding range and payload capacity. A WIGE aircraft is defined by the International Maritime Organization (IMO) as a vehicle supporting its main operation solely by aerodynamic forces and operating at low altitudes above the sea surface without any direct contact. These vehicles enable a high-performance flight benefiting from the ground-effect (GE) phenomenon, a special topic in aerospace engineering that refers to the aerodynamic, aeroelastic, and aeroacoustic impacts on platforms flying in close proximity to an underlying surface. While performing a flight near the ground (i.e., surface, ground or water), the flow field underneath the wing is trapped, placing high pressure on the lower surface (ram effect), which provides a higher lift and lower induced drag, resulting in a higher lift-to-drag ratio, namely, aerodynamic performance. In this case, the flight height of the aircraft plays a determinative role in the effectiveness of this phenomenon. The lift-to-drag

ratio of a seaplane or a light aircraft is around 8 to 12; however, a WIGE aircraft could achieve a value of 20 or higher while flying at an optimal height [19]. The history of these high-performance aircraft dates back to the early 1930s, when the initial attempt was made by Finnish engineer T. Kaario, following the first scientific efforts to describe the influence of the ground effect on airflow behavior [20,21]. However, the first major WIGE aircraft development program in history, Ekranoplan, was started in Russia in the 1960s [22]. From these attempts up until the recent past, some commercial concepts and designs, but mostly military ones, have been under development, and have been the subject of multidisciplinary investigations [23–27].

On the other hand, missions within maritime traffic necessitate the consideration of potential collision avoidance strategies, due to the simultaneous operation of WIGE aircraft and waterborne craft and any other moving or fixed obstacles. In this context, a number of methods may be employed with the purpose of obstacle avoidance, including sensor-based detection (i.e., infrared, radar, or sonar), computer vision, and autonomous navigation. Irrespective of the method employed, it is essential to investigate and enhance the performance of the system in order to minimize the risk of collision and improve the robustness of the vehicle control system response. The robustness of the autonomous control system could be defined in terms of its transient response parameters while it is tracking predefined trajectories as obstacle avoidance scenarios. Accordingly, enhancements in transient response parameters enable the improvement of obstacle avoidance performance (i.e., trajectory tracking performance).

From an engineering point of view, designing an aircraft that can achieve such a long range, together with a high payload capacity, is challenging and involves various difficulties which the current designs in the literature are mostly incapable of overcoming. Firstly, the limited number of historical data available for use as a reference lead to more difficult decision-making processes in the conceptual design of an original configuration for an aircraft like this. Furthermore, the sophisticated aerodynamics require the consideration of more specialized approaches. In investigations into the flight dynamics of an innovative design benefiting from ground-effect phenomena, dynamic model construction is a complex issue, due to the large amount of variation in aerodynamic characteristics based on flight altitude. Since missions are performed within maritime traffic, as mentioned, control system robustness is another issue that should be considered in the conceptual design. Therefore, a key challenge is to develop a multidisciplinary optimization process for the control system and the aerodynamic design of the vehicle, considering the obstacle avoidance issue, as well as ensuring range and payload capacity requirements.

Hence, the current paper introduces a conceptual design process for a novel WIGE UAV tailored to an autonomous water sampling mission for the first time in the literature. Here, a cutting-edge solution is proposed for a cost-effective, time-saving, eco-friendly, high-capacity, and long-range water sampling operation, to contribute to global environmental sustainability efforts and pave the way for innovative future studies. This research is expected to contribute to the literature through the implementation of this concurrent engineering approach and reveal the potential of this type of interdisciplinary coordination in the initial step of an aircraft design process. In this context, the design process employed an artificial neural network-integrated concurrent engineering approach combining various disciplines from a collaborative perspective, to improve a vehicle's obstacle avoidance ability in terms of its trajectory tracking performance.

2. Conceptual Design Methodology

In the aircraft design process, there are various challenges to be met and overcome within the stages of conceptual design, preliminary design, and detail design [28]. In the conceptual design stage, the rough assessment of the candidate configurations and trade studies are performed, with design requirement considerations, using low-fidelity numerical tools. The output of this phase is the single best design within a determined set of requirements. In the preliminary design stage, the determined concept is comprehensively

investigated with more advanced methods and tools, refining it in collaboration with various disciplines. This prepares the design for the detail design phase, which covers the design of the actual parts to be fabricated and assembled.

From the conceptual design point of view, the conventional process begins with the definition of the design requirements, which are the guidelines or specifications that shape the design process, such as the range, payload capacity, speed limitations, and mission profile, within the current technological availability. According to the determined requirements, the most important calculation, the sizing begins, which refers to the rough estimation of the dimensions and weight of the aircraft. This step is carried out simultaneously with the initial layout (i.e., arrangement) decisions regarding the internal and external components, to allow the determination of the location of the vehicle's center of gravity. Based on the estimated weight and location of the center of gravity, aerodynamic considerations come to the fore, with the aim of meeting the basic flight performance metrics defined in the design requirements.

In a conventional process, the control system and aerodynamic designs are usually carried out separately at this stage. Within the scope of this study, the flow was revised with an integrated product development (concurrent engineering) approach, and these disciplines were combined to be assessed simultaneously, aiming for an improvement in obstacle avoidance performance. Moreover, as a novel application, the dynamic model of the vehicle was estimated with neural network assistance. The process concluded with flight simulations to test the obstacle avoidance performance in terms of the transient response characteristics of the final design.

A block diagram of the process followed within the scope of this study is presented in Figure 1. The dashed lines in the flowchart indicate the repeatability of the process and the revisability of the design in the case of obtaining unsatisfactory performance metrics, according to the design requirements.

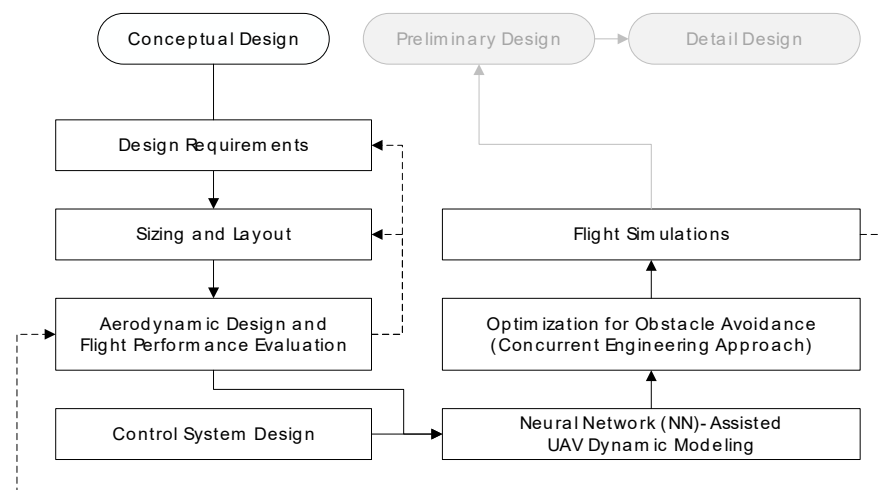


Figure 1. Conceptual design flowchart to be followed for WIGE-WS.

In the following sections of the article, the conceptual design process will be initialized, with the definition of the design requirements, followed by the estimation of the weight components and the determination of the initial layout, as mentioned in this figure. The initial exterior design and configuration of the aircraft will be described with reference to aerodynamic analyses and flight performance assessments. Simultaneously, the autonomous flight control system (AFCS) will be designed and optimized for enhancing obstacle avoidance, taking the cruise flight altitude and control system parameters into account. To perform flight simulations of the obstacle avoidance scenarios, longitudinal and lateral dynamic models will be constructed with the assistance of an artificial neural network.

2.1. Design Requirements

The design requirements for an aerial vehicle encompass a wide range of considerations, such as performance, structure, safety, environment, airworthiness, autonomy, stability, and control. In the case of a water sampling mission, the storage capacity (i.e., payload) and the range are prior considerations to be discussed.

İskenderun is a desirable location for a sampling mission, as a city with bay and port regions that provide shelter for a rich biodiversity of aquatic fauna and flora, where water sampling operations play a crucial role from both an ecosystem and economic perspective. With the aim of designing an aircraft capable of sampling in İskenderun Bay, a minimum range of 80 km was defined, to reach almost every location in the bay by taking off from stations in the Arsuz and Payas districts, as visualized in Figure 2. In order to achieve high-capacity sampling, 5 L of water storage capacity was defined, coinciding with the mission of WIGE-WS. Furthermore, a cruise airspeed (V_C) of 80 km/h was defined [23], and the corresponding endurance (E) was set at approximately 1 h for one entire mission.

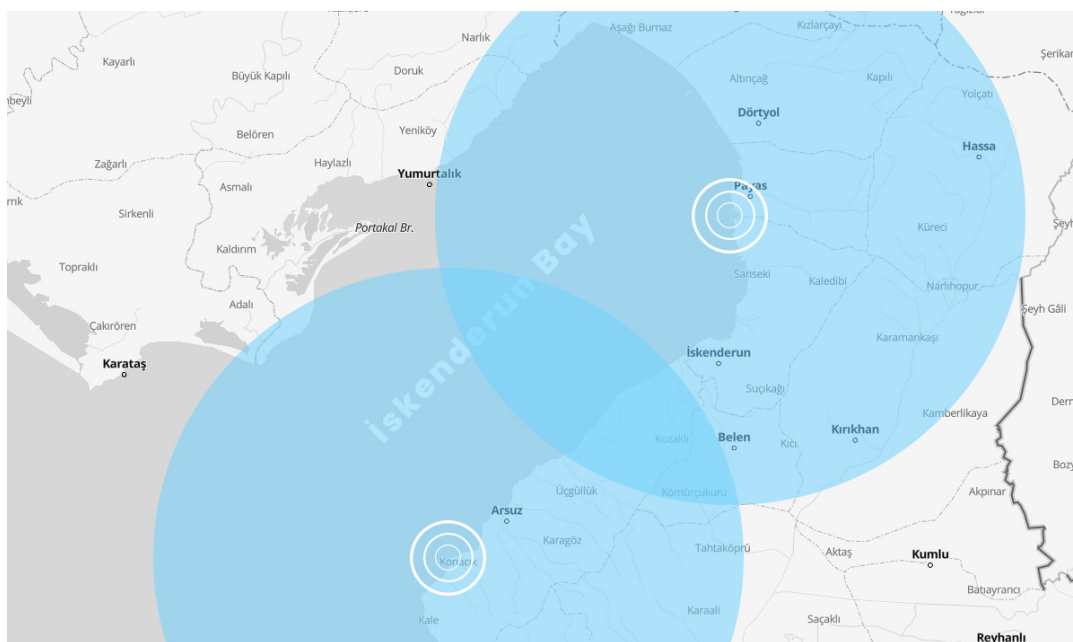


Figure 2. The range of WIGE-WS from the take-off points in Arsuz and Payas.

The flight altitude (h) of a wing-in-ground-effect aircraft has a deterministic role in flight performance, and is commonly associated with the main wing mean-aerodynamic-chord length (c) or wingspan (b). Historical trends in the ground clearance (h/c) of various aircraft designs suggest values of around 25–30% [22,23,27], but there are restrictive environmental conditions in our scenario, as well as issues to be considered in terms of operational safety, such as sea waves. The annual mean sea-wave height in İskenderun Bay is approximately 0.3 m [29,30], and, accordingly, WIGE-WS should have a higher cruising height to operate safely. Since the flight altitude and control system parameters will be optimized in further sections of this study, a flight altitude of 0.6 m ($h/c = 1$) is defined as the initial value.

The categories of the wing-in-ground-effect aircraft are divided into three subdivisions by the International Maritime Organization (IMO), Type A, Type B, and Type C, with respect to their operational capabilities. Type A is only capable of performing flight-in-ground-effect (IGE) operations, while Type B is able to jump over obstacles up to 150 m in addition to achieving sustained IGE flight and Type C is capable of performing sustained flight with both IGE and out-ground-effect (OGE) [22,31]. With the aim of designing a Type B aircraft, we decided to include a climbing (fly-over) capability for obstacle avoidance up to the height limit of 150 m (h_a) as a design requirement.

The initial design requirements are summarized in Table 1 and can be revised or improved in the later stages, according to the nature of the conceptual design process.

Table 1. Initial design requirements for WIGE-WS.

Design Requirement	Value	Unit
Cruise airspeed	80	km/h
Flight altitude	0.6	m
Range	80	km
Endurance	1	h
Water sampling capacity	5	L
Fly-over height for obstacle avoidance	150	m

Mission Profile

An aircraft is always designed to successfully perform a mission that is defined according to the design requirements. Therefore, a realistic and clear definition of the mission profile represents a critical step in the conceptual design phase. The definition is usually represented schematically, in a mission profile, which contains the essential details of the flight phases to be performed (such as altitude, range, and endurance).

The water sampling mission profile for WIGE-WS is visualized in Figure 3. The vehicle is supposed to take off from the water surface, cruise at an altitude of h , and finally land at the destination water sampling point, which is at a maximum 35 km distance. The sampling apparatus is to be released from the fuselage by means of a motor, and the water sample is to be pumped to the sample tanks. Following the sampling and the collection of the apparatus, the same route is expected to be tracked autonomously by the vehicle, so that it lands around the take-off point.

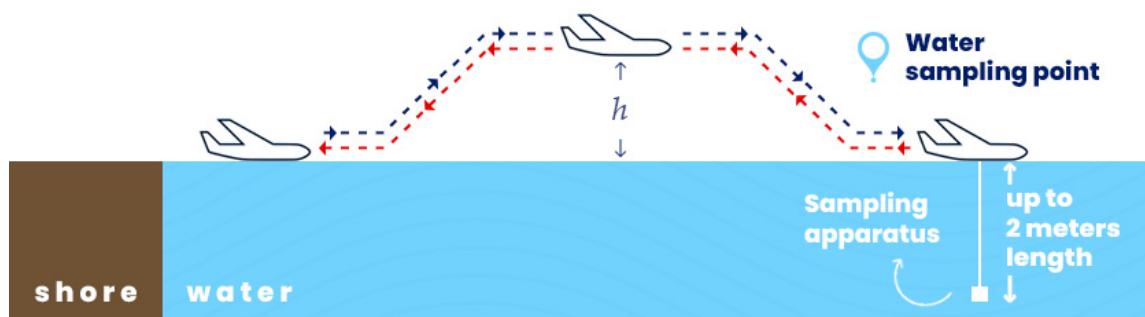


Figure 3. Water sampling mission profile.

When the aircraft faces an obstacle, the obstacle detection system identifies the distance between the aircraft and the obstacle, together with its size. Then, the aircraft needs to respond in some way, to avoid the collision. Therefore, the mission profile in the case of a flight path including an obstacle is shown in Figure 4, with two avoidance options. The first avoidance option is the fly-over mode, that is, climbing to a safe altitude of h_a with a climb angle of θ_a and descending to the cruise flight altitude after passing the obstacle. Alternatively, in the case of higher obstacles, the vehicle has the option of the maneuver mode, that is, rolling with an angle of ϕ_a and avoiding the obstacle without any change in flight altitude. In the initial version of WIGE-WS, obstacle avoidance is achieved via 5-degree climbing and 5-degree level-turn modes; these options could be revised in future versions of the vehicle.

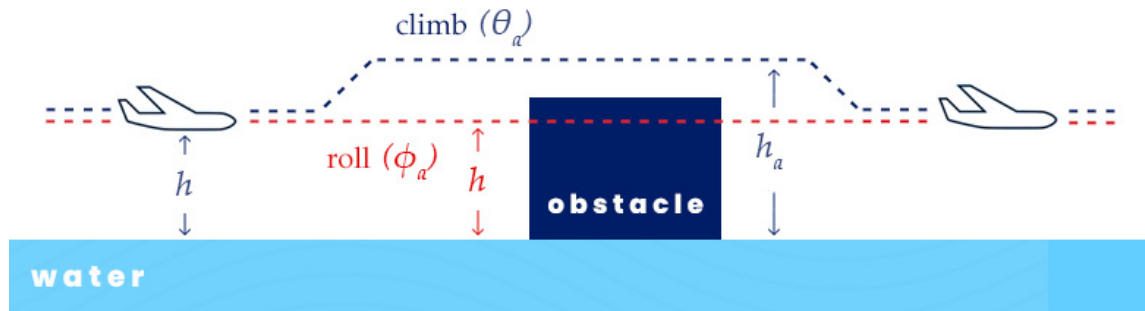


Figure 4. Obstacle avoidance mission profiles: fly-over and maneuver modes.

2.2. Sizing and Layout

The initial sizing process for an aircraft covers the rough estimation of the weight variables and vehicle dimensions that satisfy the design requirements. In this section, the weight estimations for each component of WIGE-WS are estimated via a conceptual design approach, mostly relying on historical trends, designer experience, and market research. Then, the component layout and initial dimensions of the vehicle are defined by means of aerodynamic and flight performance analyses.

2.2.1. Maximum Take-Off Weight Estimation

The maximum take-off weight (W_{MTO}) of an electric-powered autonomous aerial vehicle comprises the payload weight (W_{PL}), autopilot weight (W_A), battery weight (W_B), and empty weight (W_E). The estimation of the maximum take-off weight requires each weight component to be determined sensitively. While the payload and autopilot weights are determined at the design requirement phase, the empty weight and battery weight estimations rely on unitless weight fractions, as given in Equation (1).

$$W_{MTO} = \frac{W_{PL} + W_A}{1 - \left(\frac{W_B}{W_{MTO}}\right) - \left(\frac{W_E}{W_{MTO}}\right)} \quad (1)$$

In order to obtain the battery weight fraction, the battery weight can be estimated from Equation (2), where R is the range in m , g is the gravitational acceleration in m/s^2 , E_D is the battery energy density in Ws/kg , P is the required power in W , V is the cruise airspeed in m/s , and η is the unitless propeller efficiency [32].

$$W_B = \frac{RgP}{E_D V} \quad (2)$$

While the energy density of the battery is based on the decision of the designer, the required power can be obtained from Equations (3) and (4) via the initial estimation of the aerodynamic performance of the vehicle (L/D) by an iterative process.

$$\frac{W_{MTO}}{T} = \frac{L}{D} \quad (3)$$

$$T = \frac{P\eta}{V} \quad (4)$$

In the conceptual design phase, the empty weight fraction can only be estimated from historical trends using an empirical formulation, such as that given in Equation (5), which leads to an iterative process for obtaining the maximum take-off weight [32].

$$\frac{W_E}{W_{MTO}} = -0.00296W_{MTO} + 0.87 \quad (5)$$

Consequently, the estimated values of the design variables and weight components are presented in Table 2, following the pre-defined design requirements, historical trends, and the methodology prescribed above.

Table 2. Estimated weight and design variables of WIGE-WS.

Design Variable	Estimated Value	Unit
E_D	200	Wh/kg
η	0.7	-
L/D [22,24]	15	-
T_{req}	1.23	kg
W_B/W_{MTO}	0.11	-
W_E/W_{MTO}	0.61	-
W_A [32]	0.25	kg
W_P	5	kg
W_{MTO}	18.40	kg

2.2.2. Aerodynamic Design, Sizing, and Flight Performance Evaluation

The estimation of the maximum take-off weight paves the way for the aerodynamic design of the aerial vehicle, relying on basic flight mechanics knowledge. In this context, considering the longitudinal forces of lift (L) and weight, it should be ensured that Equation (6) is met for a steady cruise flight at a constant flight altitude and airspeed, where S is the wing area in m^2 , C_L is the lift coefficient, and ρ is the air density in kg/m^3 . Similarly, from the perspective of the lateral forces, Equation (7) provides the relation between the drag force (D) and required thrust, where C_D is the drag coefficient. A successive aerodynamic design usually needs to provide high lift together with low drag, resulting in a high lift-to-drag ratio.

$$L = W_{MTO} = \frac{1}{2}\rho SV^2 C_L \quad (6)$$

$$T = D = \frac{1}{2}\rho SV^2 C_D \quad (7)$$

In Equation (6), the air density is $1.225 kg/m^3$, which is the sea-level value, since the aircraft flies above the sea. The airspeed was defined earlier in the design requirements as $22.22 m/s$, and the estimated maximum take-off weight equals the lift force that the aircraft needs in order to perform level flight. In this context, the only unknowns that remain to be evaluated in the equation are the wing area and lift coefficient. During this step, a design lift coefficient should be determined, which the main wing is expected to generate under nominal conditions. From the perspective of sizing, wing area (S) and wing loading (W/S) are also critical parameters, with a dramatic effect on aircraft aerodynamics. Low wing loading usually leads to an improved low-speed performance and higher lift-to-drag ratio, together with better maneuverability at lower airspeeds, which is desirable in our mission. To make an appropriate choice for both, the design lift coefficient was estimated as 0.5 , which is a typical value for a subsonic aircraft, and an expected value for an IGE cruising flight benefiting from the lift contributions of the ground effect. Correspondingly, the wing area has been calculated as $1.19 m^2$ using Equation (6), and the wing loading of the vehicle is $15.41 kg/m^2$.

The drag coefficient in Equation (7) is theoretically the sum of two components, the zero-lift drag coefficient, C_{D0} , and the induced drag coefficient, C_{Di} , as given in Equation (8). The induced drag coefficient could be obtained via Equation (9), where e is the Oswald efficiency factor and AR is the wing aspect ratio obtained via Equation (10).

$$C_D = C_{D0} + C_{Di} \quad (8)$$

$$C_{D_i} = \frac{C_L^2}{\pi A R e} \quad (9)$$

$$AR = \frac{b^2}{S} \quad (10)$$

The zero-lift drag relates to the overall shape of the aircraft, while the induced drag forms due to the wingtip vortices and is related to C_L , AR , and e , as can clearly be seen in Equation (9). The definition of the wingspan is determinative in AR , with the wing area defined as above. The Oswald efficiency factor is related to the spanwise lift distribution and indicates the efficiency of the wing in producing lift with minimum drag. In order to have adequate efficiency, the wing taper ratio (λ) given in Equation (11) can be adjusted, conserving the defined wing area. Moreover, applying an anhedral angle is also known to reduce induced drag.

$$\lambda = \frac{c_{tip}}{c_{root}} \quad (11)$$

Based on the discussion above, the wing aspect ratio was determined to be 3.7 by means of following the suggestions in the literature for maximizing the advantage from the ground effect [22,24,27] and, consequently, the wingspan (b) and mean aerodynamic chord of the wing were set as 2.1 m and 0.6 m, respectively, and the cruise flight height was set as 0.6 m, due to the ground clearance defined in the design requirements. Finally, the wing taper ratio was determined as 0.45 (with the tip section excluded), which was known to provide a satisfying lift distribution [28].

The airfoil in the root section of the main wing was determined to be NACA 4412, relying on its well-known aerodynamic characteristics, especially its superiority in terms of high lift-to-drag ratio. Furthermore, NACA 0015 was selected for the tip section, with the objective of providing support for the vehicle to float on the water surface without generating any additional lift force that would disturb the aircraft. In the empennage, the symmetrical NACA 0012 airfoil was preferred for both vertical and horizontal tails; this is a typical symmetrical airfoil which is commonly used, due to the fact that it does not produce remarkable pitching moments at low angles in attack flights, which was desired.

The sizing of the empennage components (i.e., horizontal and vertical tail) were carried out with respect to the volume coefficients given in Equations (12) and (13), where l_v is the vertical tail arm length in m , l_H is the horizontal tail arm length in m , S_v is the vertical tail area in m^2 , b is the wingspan in m , and S_H is the horizontal tail area in m^2 [28,32].

$$\bar{V}_V = \frac{l_v S_v}{b S} \quad (12)$$

$$\bar{V}_H = \frac{l_H S_H}{\bar{c} S} \quad (13)$$

The volume coefficients are determinative in the stability characteristics of the vehicle; the horizontal coefficient effects the longitudinal stability, and the vertical coefficient effects the lateral-directional stability. For instance, a higher V_H means a larger and more effective horizontal tail surface, which results in a greater longitudinal stability that counters pitching moments. The typical values of V_H are between 0.65 and 0.85, while V_V values are between 0.05 and 0.1 for conventional aircraft [32].

The lengths of the vertical and horizontal tail arms were initially determined, through an empirical methodology, to be approximately 60% of the length of the fuselage. To fulfill the condition for longitudinal static stability in the aircraft, the pitching-moment coefficient curve slope, $C_{m\alpha}$, should have a negative value and the reference pitching-moment coefficient should have a positive value, which are sensitive to tail arm lengths. In this context, the arm lengths were adjusted and V_V and V_H were obtained as 0.072

and 0.655, respectively, in order to have a moderate stability characteristic together with controllability.

The dimensions of control surfaces (i.e., the elevator, rudder, and ailerons) were determined based on their effectiveness, which was defined as the ratio of the control surface area to the lifting-surface area. The initial definitions of the effectiveness of the aileron, rudder, and elevator were set at the moderate values of 0.5, 0.4, and 0.4, respectively [33].

In the conceptual design phase, the flight performance of an aircraft is initially investigated via low-fidelity tools, such as vortex lattice solvers, rather than high-fidelity but time-consuming Navier–Stokes solvers or expensive wind-tunnel experiments. Within the scope of the aerodynamic assessment of the vehicle, XFLR5 v6.61 is a useful public licensed software that facilitates rapid results with satisfactory accuracy using the vortex lattice method (VLM), lifting-line theory (LLT), or 3D panel method [34,35]. In VLM analysis, the surfaces of the aircraft are constructed with panels that comprise infinite vortices to estimate aerodynamic characteristics such as the lift-curve slope or induced drag [36]. As a finite-element application, it is useful to conduct the grid independence investigation at the beginning of the analysis, to obtain the optimal computational time and accuracy, independently of the number of VLM panels.

The grid-independence analyses were performed using viscous ring vortex analysis at 80 km/h airspeed (i.e., a Reynolds number of 9.12×10^5 with respect to MAC) and a flight altitude of 0.6 m constructed with various numbers of VLM panels and results are given in Figure 5.

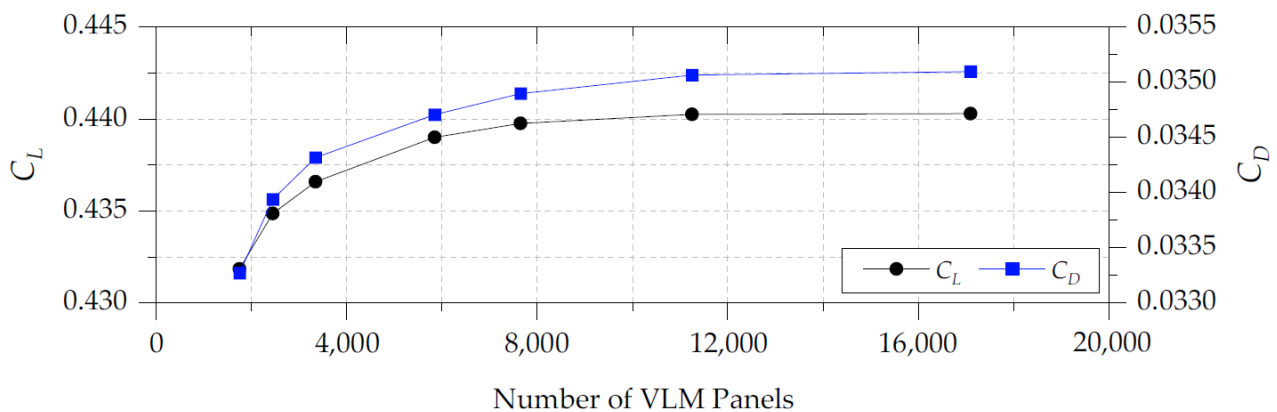


Figure 5. WIGE-WS grid independence results for cruising flight at $h/c = 1$.

The C_L and C_D results obtained utilizing 5850 and 17,100 VLM panels were found to exhibit a discrepancy of 0.292% and 1.12%, respectively. Therefore, the final model constructed utilizing 5850 panels for further analyses and the distribution of the panels are illustrated in Figure 6. An initial analysis of steady-level flight in WIGE-WS was carried out, and the results are given in Table 3, where C_{L0} is the reference lift coefficient and C_{M0} is the reference pitching-moment coefficient.

Table 3. Aerodynamic characteristics of WIGE-WS for steady-level flight at $h/c = 1$.

Parameter	Value
C_{L0}	0.4403
C_{D0}	0.0351
C_L/C_D	12.544
C_{M0}	0.0961
e	0.483

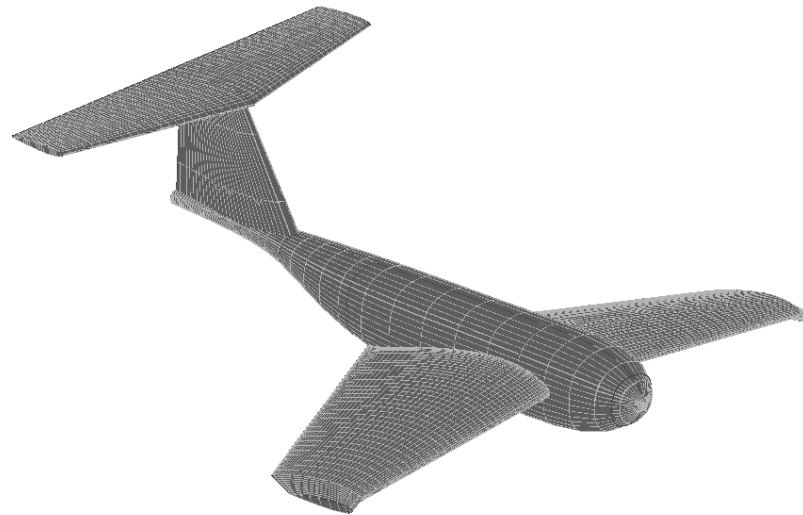


Figure 6. VLM panel distribution on WIGE-WS.

Taking the initial take-off weight of WIGE-WS into account, which does not include the weight of the water sample, the range must be estimated separately for two flight phases using the revised version of the Breguet range equation for electrically powered aircraft given in Equation (14), where g is the gravitational acceleration and W_i is the total weight of the aircraft for each flight phase.

$$R_i = \frac{E_D}{g} \frac{C_L}{C_D} \frac{W_B}{W_i} \eta \quad (14)$$

Since the weight of the aircraft at the beginning of the flight does not include the payload, the range was obtained using W_E and defined as R_1 . Subsequent to a successful water sampling operation, the weight of the vehicle reached its maximum take-off weight, and then the range was estimated using W_{MTO} and defined as R_2 . Based on the estimated battery weight fraction and aerodynamic performance results provided in Table 1, the range of the aircraft could be obtained by averaging R_1 and R_2 and was found to be 87.81 km, which meets the design requirements given in Table 1. It should be noted that the weight of the battery was increased by 10% to ensure that it could withstand the additional drag due to the seawater environment. The initial flight performance metrics are summarized in Table 4.

Table 4. Initial flight performance metrics of WIGE-WS.

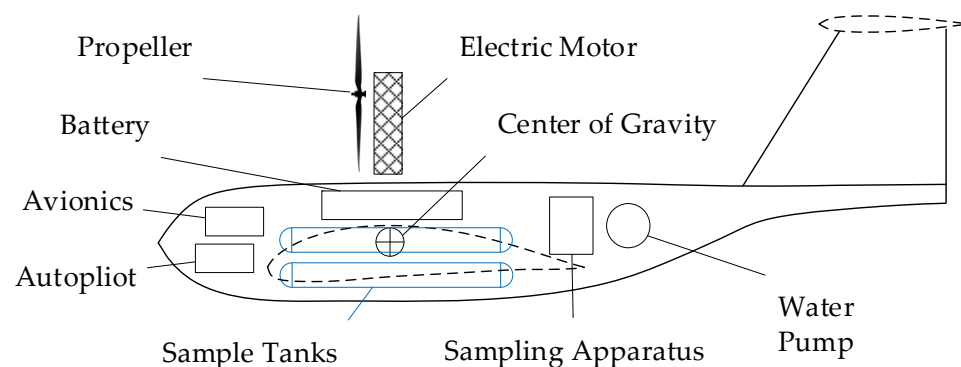
Parameter	Value	Unit
R_1	77.09	km
R_2	98.52	km
R_{AVE}	87.81	km
V_C	85.32	km/h
E	1.03	h

The electric-powered propulsion system of WIGE-WS was required to provide a minimum thrust of 1.23 kg, according to the analysis results for cruising flight with the maximum take-off weight. In this context, a 26-inch diameter propeller (26 × 8.5) that is capable of reaching angular speed up to 12,000 RPM and an electric motor with a maximum power of 2.7 kW were used, capable of providing a static thrust of 3.59 kg at 50% throttle and 12.1 kg maximum static thrust at full throttle, which were adequate for our mission. The component-weight distribution of WIGE-WS is summarized in Table 5.

Table 5. Component weights of WIGE-WS.

Component	Weight (kg)
Fuselage	1.50
Main wing	1.40
Horizontal tail	0.90
Vertical tail	0.80
Payload	5.00
Sampling apparatus (motor included)	1.35
Water pump	0.45
Sample tanks	0.50
Electric motor and propeller	0.90
Battery	2.20
Autopilot and ESC	0.10
Obstacle detection sensors	0.80
Cabling	0.80
Control surfaces	0.60
Internal support elements	0.60
Total	18.40

The internal and external layout of the main components are illustrated in Figure 7. In this allocation, the center of gravity (CG) of the aircraft is positioned at a distance of 0.406 m from the leading edge of the main wing. In order to ensure that the center of gravity remained consistent throughout the mission, the components with the highest weight, namely, the electric motor and battery, and particularly the sample tanks, were positioned on the same axis, horizontally along the CG.

**Figure 7.** Internal- and external-component layout of WIGE-WS.

The aerodynamic investigations were carried out at various flight altitudes with a defined CG position to examine the effectiveness of the ground effect on aircraft aerodynamics and stability, and the detailed results for cruising at the Reynolds Number are presented in Figure 8. The decrease in flight altitude dramatically shifted the lift and lift-to-drag ratio curves upwards, especially for ground clearance values lower than 0.4. At any altitude, the vehicle provided the design lift coefficient via variation in the reference angle of attack of up to 3 degrees, even in OGE flights. At low-altitude IGE flights, the slight decrement in the drag coefficient combined with the substantial increment in the lift coefficient resulted in a dramatic increase in the lift-to-drag ratio, reaching a value approximately two times higher than that for the OGE ($h/c = 1.5$). The tendency of the results was found to be in good agreement with similar experimental and numerical studies in the literature [27,37,38].

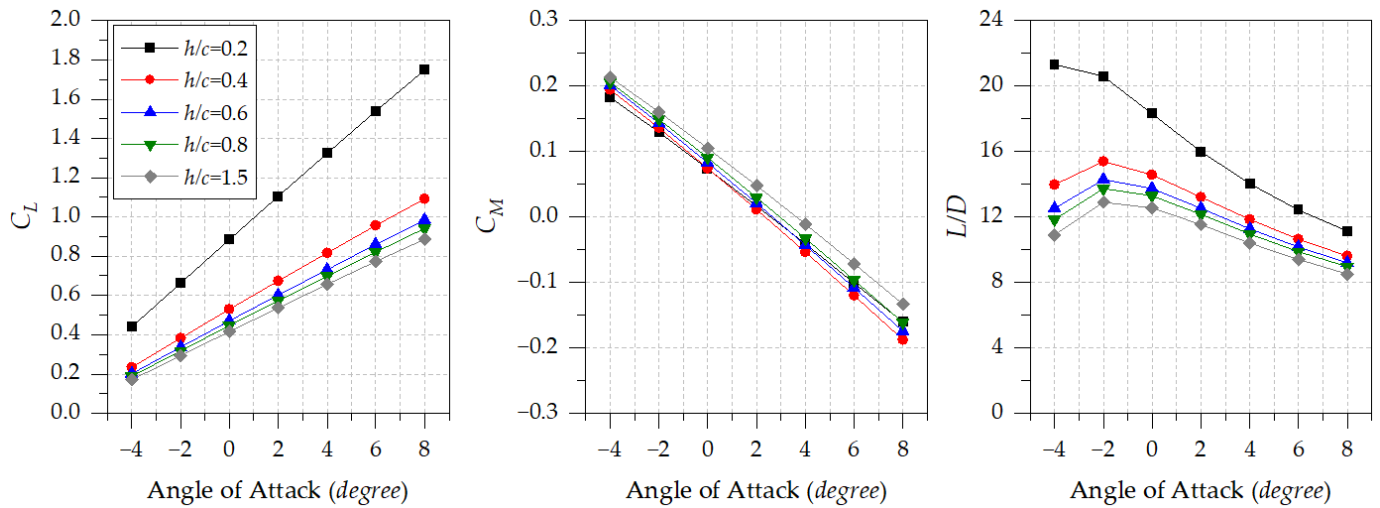


Figure 8. The aerodynamic analysis results for steady-level flight at $h/c = 1$ at various angles of attack.

The pitching–moment curve was shifted upwards with the increment in flight altitude, which refers to improvements in the static longitudinal stability at higher altitudes. Overall, the IGE and OGE flight conditions resulted in a similar negative pitching–moment–curve slope tendency, and showed satisfying stability characteristics. The trim angle of attack showed a slight variation of 2 degrees within the flight altitude range. Consequently, the finalized external design and dimensions of WIGE-WS are presented in Figure 9. It should be kept in mind that this design relies on results obtained using low-fidelity tools, and should be more precisely investigated in the preliminary design stage.

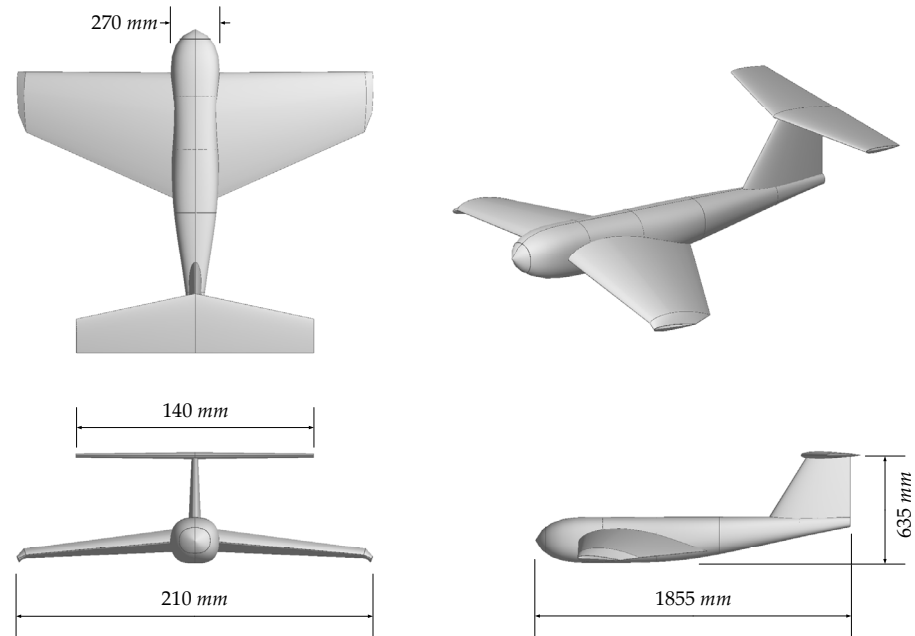


Figure 9. External dimensions and CAD drawing of WIGE-WS.

2.3. Autonomous Flight Control System (AFCS) Design

The autonomous flight control system was designed as a traditional hierarchically structured proportional–integral–derivative (PID) controller consisting of six PID controllers, as shown in Figure 10. The system is composed of three layers, referred to as the outer, middle, and inner layers, each with specific responsibilities regarding the altitude, airspeed, and heading of the vehicle.

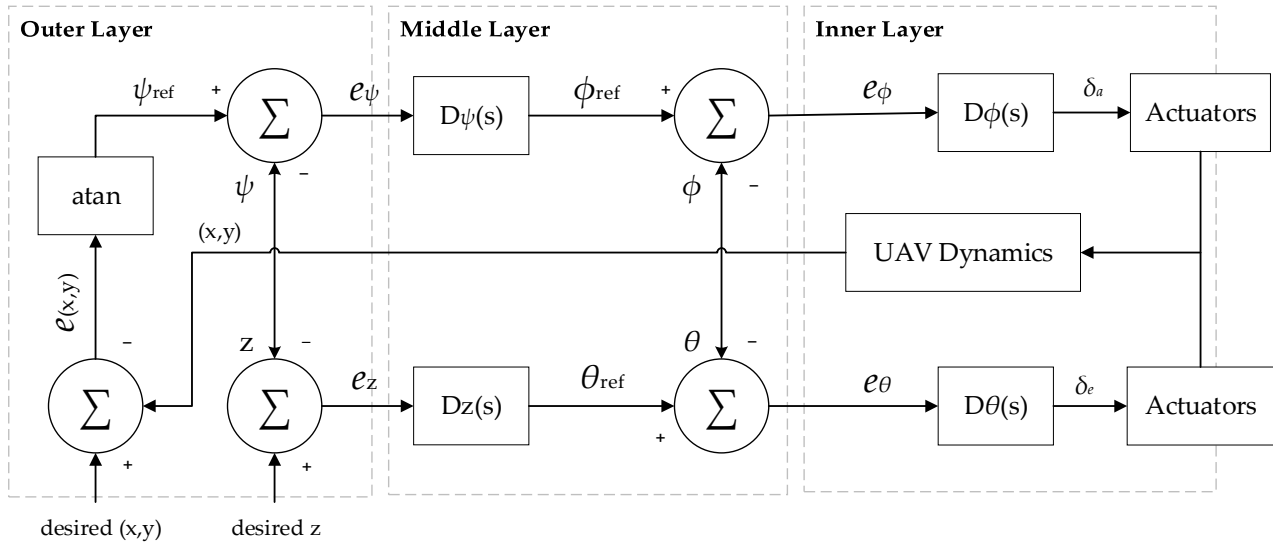


Figure 10. Block diagram of the AFCS.

The inner layer is responsible for the stabilization of the roll and pitch attitudes, considering the variation in the elevator and aileron control surface deflections, δ_e and δ_a , as given in Equations (15) and (16), where θ and ϕ are the instantaneous pitch and roll angles, e_θ and e_ϕ are the errors (the difference between the instantaneous and reference values) in the pitch and roll angle, and p and q are the roll and pitch rates, respectively. Moreover, the proportional, integral, and derivative gains for the controllers related to longitudinal and lateral motions are defined as $K_{P_{LON}}$, $K_{I_{LON}}$, $K_{D_{LON}}$ and $K_{P_{LAT}}$, $K_{I_{LAT}}$, and $K_{D_{LAT}}$, respectively.

$$\Delta\delta_e = -K_{P_{LON}}^\theta e_\theta - K_{I_{LON}}^\theta \int_0^t e_\theta dt - K_{D_{LON}}^\theta q \quad (15)$$

$$\Delta\delta_a = -K_{P_{LAT}}^\phi e_\phi - K_{I_{LAT}}^\phi \int_0^t e_\phi dt - K_{D_{LAT}}^\phi p \quad (16)$$

The middle layer carries out heading and altitude stabilization by providing the inner layer with the reference values for the pitch and roll angles, θ_{ref} and ϕ_{ref} , as shown in Equations (17) and (18), where h is the flight altitude, ψ is the yaw angle, e_h and e_ψ are the errors (the difference between the instantaneous and reference values) in altitude and yaw angle, V_D is the descent rate, and r is the yaw rate.

$$\theta_{ref} = -K_{P_{LON}}^h e_h - K_{I_{LON}}^h \int_0^t e_h dt - K_{D_{LON}}^h V_D \quad (17)$$

$$\phi_{ref} = -K_{P_{LAT}}^\psi e_\psi - K_{I_{LAT}}^\psi \int_0^t e_\psi dt - K_{D_{LAT}}^\psi r \quad (18)$$

The outer layer performs the x-y position tracking of the aerial vehicle and provides the middle layer with the true heading reference input, ψ_{ref} , to track the waypoints defined for the mission.

2.4. Aircraft Dynamic Modeling

In the field of aeronautical engineering, the dynamic model of an aircraft is a mathematical model that provides an accurate representation of the vehicle's dynamic characteristics, such as stability and controllability, and provides a framework for analyzing and predicting its responses to various inputs and disturbances in different flight conditions. The develop-

ment of an appropriate and precise model plays a key role in the assessment of the flight performance and characteristics of the vehicle.

The dynamic model can be constructed using various methods, e.g., parametric modeling, multi-body modeling, flexible body modeling, or hybrid modeling approaches, each of which has its own pros and cons. The parametric modeling is a well-established method that offers the advantages of flexibility and adaptability, enables the evaluation of the trade-offs between various design parameters, and facilitates the design and tuning of control systems [33]. The method describes the nonlinear time-varying characteristics of the system using a state–space model or an input–output model.

The longitudinal and lateral dynamic models of WIGE-WS were constructed using parametric state–space modeling. The linearized model comprises force, moment, and kinematic equations of motion with state-variable representation as sets of first-order differential equations. The linearized equations are simple, ordinary linear differential equations with constant coefficients, which are composed of the aerodynamic stability derivatives and mass and inertia characteristics of the aircraft. The constructed longitudinal and lateral dynamic models are shown in Equations (19) and (20) in state–space representation, where x and u are state and control vectors and A and B are stability and control matrices, respectively. The linear velocities are represented as u , v , and w in m/s, the forces are X , Y , and Z in kgm/s², the angular velocities are p , q , and r in rad/s, the moments are L , M , and N in Nm, and the inertial terms are I_x , I_y , and I_z in kgm² with respect to the x , y , and z axes of the aircraft frame of reference, respectively. Moreover, the terms δT , δe , δa , and δr represent the throttle, elevator, aileron and rudder deflections, and θ , ϕ , and β are the pitch, roll, and sideslip angles in *rad*, respectively.

$$\underbrace{\begin{bmatrix} \Delta \dot{u} \\ \Delta \dot{w} \\ \Delta \dot{q} \\ \Delta \dot{\theta} \end{bmatrix}}_{\dot{x}_{long}} = \underbrace{\begin{bmatrix} X_u & X_w & 0 & -g \\ Z_u & Z_w & u_0 & 0 \\ M_u + M_{\dot{w}}Z_w & M_w + M_{\dot{w}}Z_w & M_q + M_{\dot{w}}u_0 & 0 \\ 0 & 0 & 0 & 0 \end{bmatrix}}_{A_{longitudinal}} \underbrace{\begin{bmatrix} \Delta u \\ \Delta w \\ \Delta q \\ \Delta \theta \end{bmatrix}}_{x_{long}} + \underbrace{\begin{bmatrix} X_{\delta T} & X_{\delta e} \\ Z_{\delta T} & Z_{\delta e} \\ M_{\delta T} + M_{\dot{w}}Z_{\delta T} & M_{\delta e} + M_{\dot{w}}Z_{\delta e} \\ 0 & 0 \end{bmatrix}}_{B_{longitudinal}} \underbrace{\begin{bmatrix} \Delta \delta T \\ \Delta \delta e \end{bmatrix}}_{u_{long}} \quad (19)$$

$$\underbrace{\begin{bmatrix} \Delta \dot{\beta} \\ \Delta \dot{p} \\ \Delta \dot{r} \\ \Delta \dot{\phi} \end{bmatrix}}_{\dot{x}_{lat}} = \underbrace{\begin{bmatrix} \frac{Y_{\beta}}{u_0} & \frac{Y_p}{u_0} & -\frac{g}{u_0} \cos(\theta_0) & -(1 - \frac{Y_r}{u_0}) \\ L_{\beta}^* + \frac{I_{xz}}{I_{xx}} N_{\beta}^* & L_p^* + \frac{I_{xz}}{I_{xx}} N_p^* & L_r^* + \frac{I_{xz}}{I_{xx}} N_r^* & 0 \\ N_v^* + \frac{I_{xz}}{I_{zz}} L_v^* & N_p^* + \frac{I_{xz}}{I_{zz}} L_p^* & N_r^* + \frac{I_{xz}}{I_{zz}} L_r^* & 0 \\ 0 & 0 & 1 & 0 \end{bmatrix}}_{A_{lateral}} \underbrace{\begin{bmatrix} \Delta \beta \\ \Delta p \\ \Delta r \\ \Delta \phi \end{bmatrix}}_{x_{lat}} + \underbrace{\begin{bmatrix} 0 & \frac{Y_{\delta r}}{u_0} \\ L_{\delta a}^* + \frac{I_{xz}}{I_{xx}} N_{\delta a}^* & L_{\delta r}^* + \frac{I_{xz}}{I_{xx}} N_{\delta r}^* \\ N_{\delta a}^* + \frac{I_{xz}}{I_{zz}} L_{\delta a}^* & N_{\delta r}^* + \frac{I_{xz}}{I_{zz}} L_{\delta r}^* \\ 0 & 0 \end{bmatrix}}_{B_{lateral}} \underbrace{\begin{bmatrix} \Delta \delta a \\ \Delta \delta r \end{bmatrix}}_{u_{lat}} \quad (20)$$

In the case of a WIGE aircraft, the flight altitude (i.e., ground clearance) substantially affects the aerodynamic characteristics and corresponding stability and control derivatives in both longitudinal and lateral dynamic models. Therefore, the flight altitude-dependent derivatives in the equations should be precisely identified and examined, to enhance the flight dynamics of the vehicle. In this context, while the inertial and geometrical variables and mass properties of the vehicle are independent from the ground clearance, the x -axis force and moment derivatives X_u , X_{α} , X_w , L_p , L_r , $L_{\delta a}$, and $L_{\delta r}$, the y -axis force and moment derivatives Y_p , M_w , $M_{\dot{w}}$, M_{α} , and $M_{\dot{\alpha}}$, and the z -axis force and moment derivatives Z_u , Z_w , $Z_{\dot{w}}$, Z_{α} , $Z_{\dot{\alpha}}$, N_p , and $N_{\delta a}$ are predominantly shaped by aerodynamic effects related to flight altitude.

For instance, in the longitudinal dynamic model, the derivative Z_w represents the variation in z -axis force with the linear velocity component on the z -axis, and can be obtained from Equation (21). As the dynamic pressure, Q , wing area, maximum take-off

mass, m , and reference airspeed, u_0 , are constant in our case, the aerodynamic variables of the lift curve slope, $C_{L\alpha}$, and zero-lift drag coefficient, C_{D0} , are the determinative parameters.

$$Z_w = \frac{-(C_{L\alpha} + C_{D0})QS}{mu_0} \quad (21)$$

On the other hand, in the lateral dynamic model, the derivative N_p represents the variation in z-axis moment with x-axis angular velocity, can be obtained using Equation (22), and simply depends on the aerodynamic variable lift coefficient.

$$N_p = -\frac{Q S b^2 C_L}{16 u_0 I_x} \quad (22)$$

Similarly to the examples mentioned above, further and extended information regarding equations for the remaining stability and control derivatives can be found in [33].

In consequence, in addition to the constant derivatives in the dynamic models, the aforementioned 19 aerodynamically dependent stability derivatives should be obtained for ground clearance values, within the constraints of this study, to construct dynamic models and examine flight performance. To facilitate this process by means of a proper artificial intelligence approach, the data could be accurately expanded to avoid the necessity of performing a huge number of aerodynamic analyses for a wide range of ground clearance values, and the prediction of stability derivatives could be achieved for every flight altitude.

Dynamic Model Prediction via Artificial Neural Network (ANN)

Artificial neural networks are a type of machine learning algorithm that have gained considerable popularity in a wide range of engineering applications for a variety of tasks (e.g., prediction, classification, and recognition), particularly over the last several decades.

As discussed in Section 2.2.2, the aerodynamic analyses of WIGE-WS were performed for a limited number of ground clearance values: 0.2, 0.3, 0.4, 0.6, 0.8, 1.0, 1.5, 2.0, 3.0, and 4.0. Therefore, during the optimization process, only the dynamic models for flights at these altitudes could be generated and examined. In order to predict longitudinal and lateral dynamic model stability and control derivatives for flights with other ground clearances, a simple feedforward neural network (FNN) architecture was constructed, aimed at data expansion, as represented in Figure 11. FNNs represent the basic type of neural networks, where connections between nodes do not form cycles, and are categorized as supervised learning. These are relatively simple compared to more complex architectures such as recurrent neural networks (RNNs) or convolutional neural networks (CNNs). The architecture typically comprises an input layer, one or more hidden layers, and an output layer, as a type of ANN.

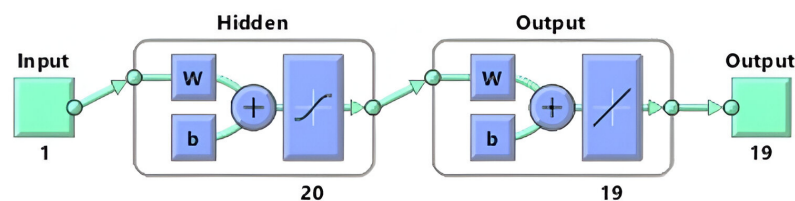


Figure 11. Block diagram representation of the constructed FNN in MATLAB.

In our case, the input layer of the FNN contains only ground clearance ($0.2 \leq h/c \leq 4.0$), the hidden layer contains 20 neurons, which was determined based on a heuristic trial-and-error method, and the output layer contains 19 neurons, corresponding to the height-dependent stability and control derivatives of the longitudinal and lateral dynamic models discussed in the previous section. In summary, the FNN takes any ground clearance value and predicts 19 stability and control derivatives, which it provides as an output.

The stability and control derivatives previously obtained for 10 different ground clearances were used to train the FNN, with 30% of the data reserved for validation. The training was carried out using the back-propagation Levenberg–Marquardt algorithm, combining stochastic gradient descent and Gauss–Newton methods, which represent a well-known fast-converging and useful approach in such simple cases [39,40]. The type of evaluation used was mean squared error (MSE), and training was completed in 16 iterations, with an overall R value of 0.9854.

2.5. Obstacle-Avoidance Performance Improvement

The obstacle avoidance process starts by detecting potential in-flight threats, assessing their impact, and, finally, implementing proper maneuvers to avoid collisions. Since the preliminary steps are not within the scope of this conceptual design study, the jump (fly-over) and level-turn (maneuver) avoidance scenarios that were previously defined in the mission profile are considered and discussed.

When the aircraft faces an obstacle, the accurate tracking of these attitudes with a robust control system response to the input signal provided by proximity sensors plays a vital role in obstacle avoidance. The performance of a control system could be described using transient response parameters such as the rise time, T_r , settling time, T_s , maximum overshoot, M_p , peak time, T_p , or damping ratio, ζ . Within these parameters, the necessity for a fast and accurate control system response brings the maximum overshoot, the rise time, and the settling time to the fore, to avoid collision. In terms of its definition, the maximum overshoot represents the peak value exceeding the desired response of the system, expressed as a percentage. The rise time represents a fundamental parameter that defines the time required to progress from 10% to 90% of the steady-state value of a step response, in seconds, while the settling time represents the time required to reach and stay within a range of 5% of the desired response of the system.

The step-response parameters could be characterized by the proportional, derivative, and integral coefficients of the longitudinal and lateral controllers presented previously. The ground clearance also has a substantial effect on the longitudinal and lateral dynamics of the vehicle. In such a case, concurrent engineering approaches could provide a significant enhancement in step-response parameters, and, accordingly, the obstacle avoidance performance could be improved via the simultaneous adjustment of the longitudinal and lateral PID coefficients (P_{LON} , I_{LON} , D_{LON} , P_{LAT} , I_{LAT} , and D_{LAT}) and flight altitude (h). Since analytical methods remain unfeasible for this type of multivariate complex problem, a gradient-free stochastic optimization algorithm must be utilized.

2.5.1. Simultaneous Perturbation Stochastic Approximation (SPSA)

SPSA is a recursive gradient-free stochastic approximation method mostly used to optimize multivariate systems composed of complex relationships, and it is known to have been applied successfully in various aerospace applications, including trajectory deviation estimation [41], flight path optimization [42], traffic monitoring and management [43,44], and control system problems [45,46]. The main advantage and superiority of this method lie in providing faster results than other conventional finite-difference approaches by performing fewer numbers of recursions to estimate the gradient and reach the global minimum for the multivariate differentiable cost function. The algorithm sustains the optimization process iteratively, starting with the initial estimation of the cost function and updating the estimations until a solution is reached. The loop of the iterative algorithm ends when the variation in the cost function stays approximately constant over a number of sequential iterations or when it has reached a defined maximum iteration number. The detailed theoretical background of, and further information about, this algorithm can be found in [47,48].

In our optimization case, the cost functions (C_{LON} and C_{LAT}) were constituted separately from the longitudinal ($T_{rLON}, T_{sLON}, M_{PLON}$) and lateral ($T_{rLAT}, T_{sLAT}, M_{PLAT}$) control system step-response parameters, as shown in Equations (23) and (24).

$$C_{LON} = T_{rLON} + T_{sLON} + M_{PLON} \tag{23}$$

$$C_{LAT} = T_{rLAT} + T_{sLAT} + M_{PLAT} \tag{24}$$

Since we aimed to obtain a simultaneous improvement in both of the avoidance scenarios, the total cost function (C_{TOTAL}) was also constituted by the summation of the longitudinal and lateral cost functions, as shown in Equation (25).

$$C_{TOTAL} = C_{LON} + C_{LAT} \tag{25}$$

Consequently, the objective of the optimization problem was formed as the minimization of C_{LON} , C_{LAT} , and C_{TOTAL} , with the constraint of ensuring that the aerodynamic performance was higher than its initial value ($L/D \geq 12.98$). For this purpose, the SPSSA optimization algorithm was coded in the MATLAB environment and integrated into the trained FNN model, as simplified and summarized in Figure 12.

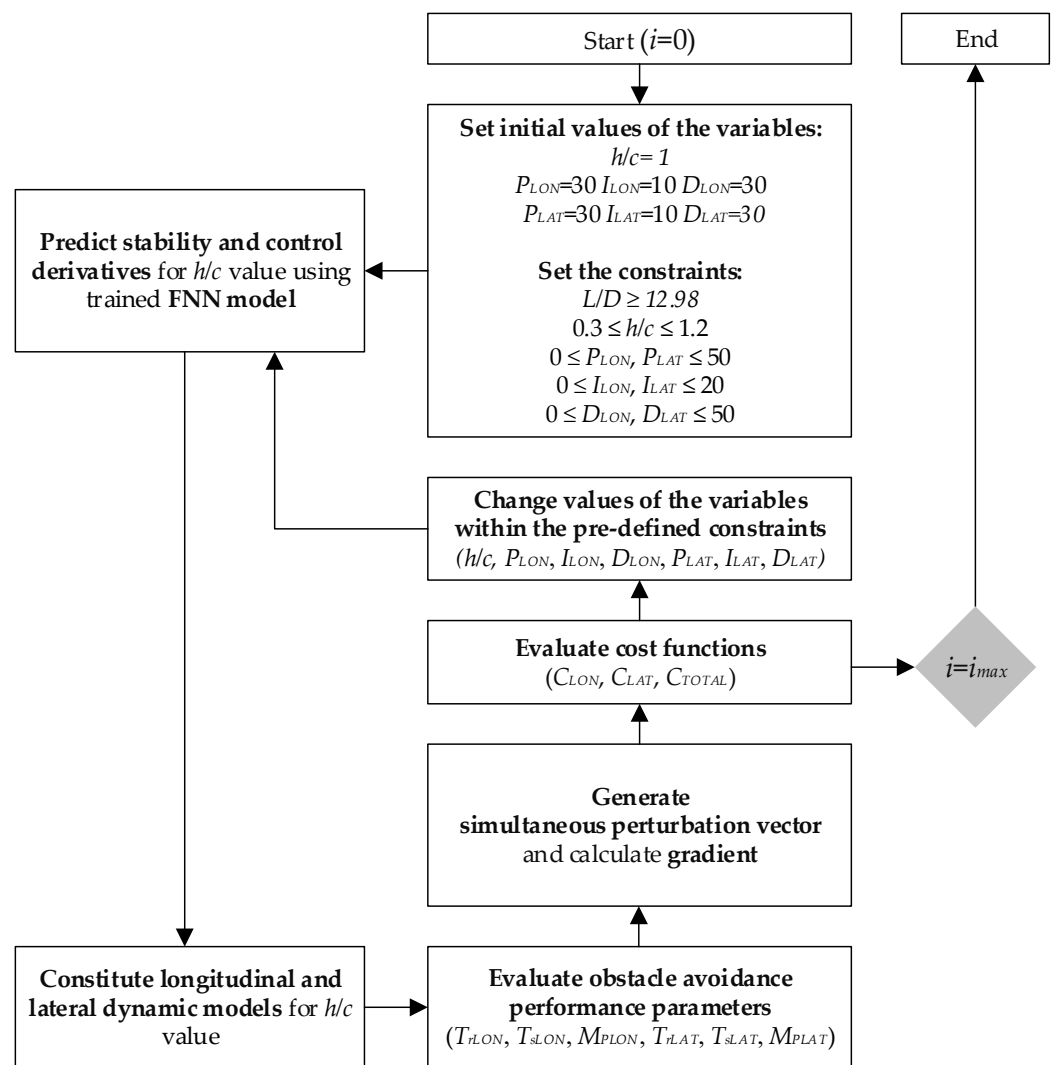


Figure 12. The block diagram of the optimization process.

The initial values of h/c and longitudinal and lateral PID coefficients were set at the beginning of the process, as stated in this figure. The constraints and maximum number of iterations ($i_{max} = 10$) were identified before initializing the algorithm, with the first iteration (i) denoted as “0”. Regarding the generated input h/c value from the algorithm, the previously trained FNN estimates the corresponding stability and control derivatives that are required to constitute longitudinal and lateral dynamic models. The dynamic models were used for the evaluation of step-response performance parameters in both obstacle avoidance scenarios, with the PID coefficients provided by the algorithm within the constraints. The optimization algorithm runs until the defined maximum number of iterations is reached.

As a result, the variation in the longitudinal and lateral PID coefficients during the optimization process is shown in Figures 13 and 14. It is clear from the figures that the algorithm converged, and kept the coefficients approximately constant after three iterations, which was expected, and demonstrates the superior characteristics of the SPSA. The variation in ground clearance and cost functions during the optimization process is shown in Figure 15, Figure 16, and Figure 17, respectively, which show a similar tendency regarding PID coefficients.

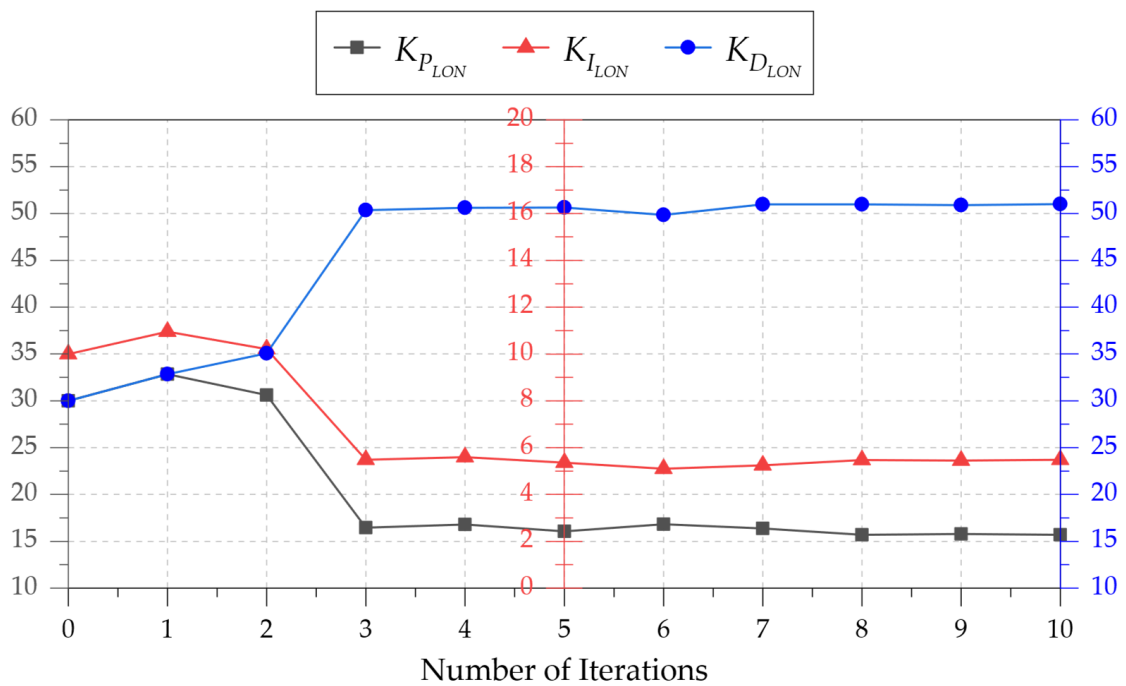


Figure 13. Variation in longitudinal PID coefficients in the optimization process.

The optimization process resulted in the minimization of the cost functions, and suggested a ground clearance value and a set of PID coefficients for improved obstacle avoidance performance. The longitudinal and lateral costs showed the remarkable reductions of 89.9% and 18.66%, while the total cost exhibited a reduction of 49.82%. Simultaneously, the aerodynamic performance of the aerial vehicle was found to be improved by 3.92%, thanks to the change in ground clearance, as was desired and defined in the constraints. The results are summarized in Table 6, in terms of the initial and optimized values of the lift-to-drag ratio, ground clearance, flight altitude, PID coefficients, and longitudinal and lateral costs.

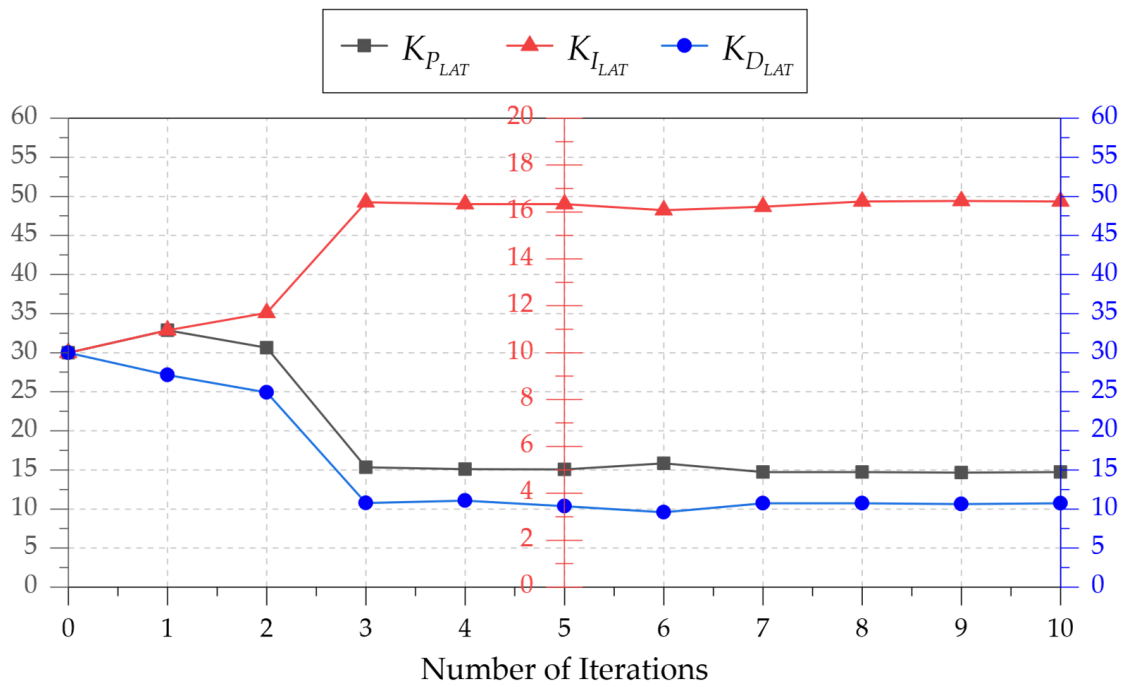


Figure 14. Variation in lateral PID coefficients in the optimization process.

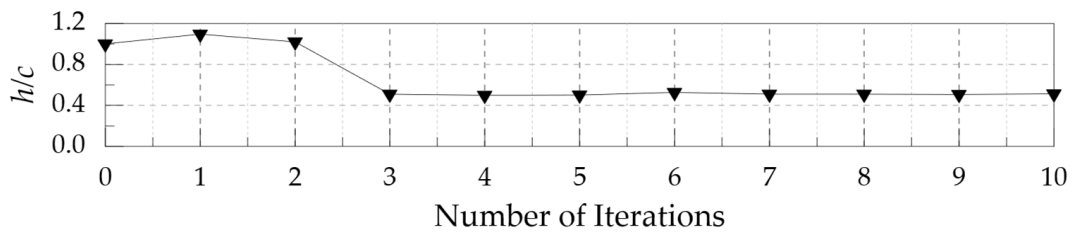


Figure 15. Variation in ground clearance in the optimization process.

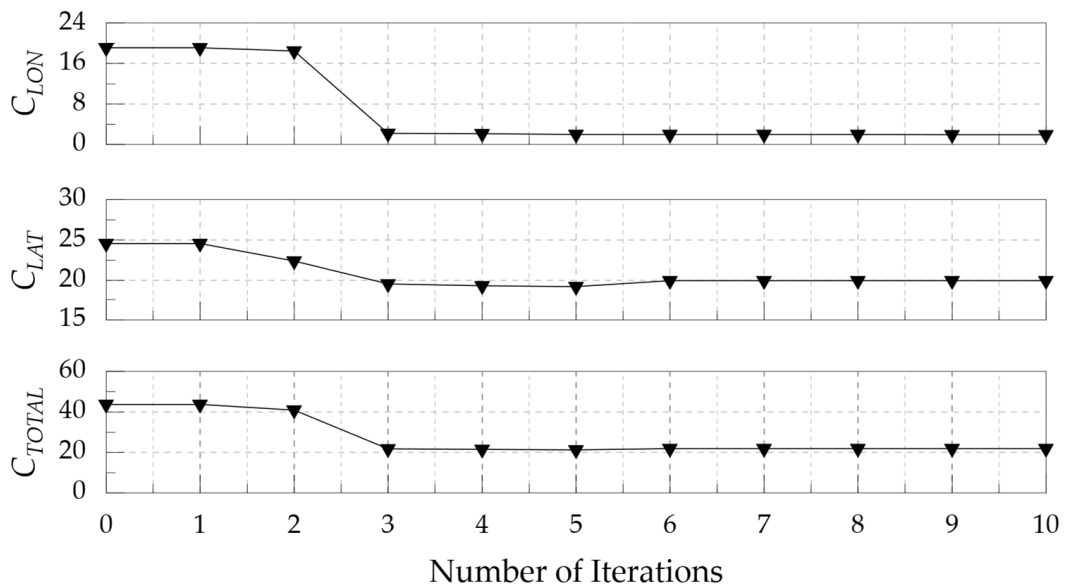


Figure 16. Variation in cost variables in the optimization process.

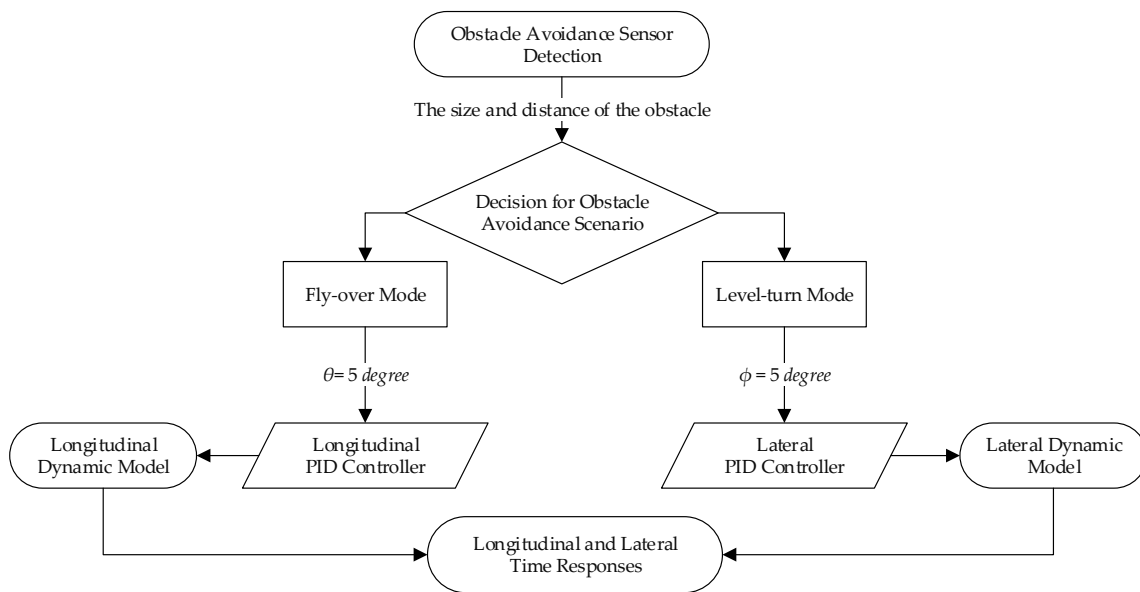


Figure 17. Block diagram of the flight simulations, including obstacle avoidance scenarios.

Table 6. SPSA optimization results.

	Initial Value	Optimized Value
Flight altitude (m)	0.6	0.307
Ground clearance (h/c)	1	0.512
Lift-to-drag ratio	12.98	13.51
Longitudinal		
Overshoot (%)	12.535	0.678
Settling time (s)	2.700	0.811
Rise time (s)	0.505	0.439
K_{PLON}	30	15.687
K_{ILON}	10	5.477
K_{DLON}	30	50.998
C_{LON}	19.090	1.927
Lateral		
Overshoot (%)	15.909	6.907
Settling time (s)	6.434	12.551
Rise time (s)	0.710	0.518
K_{PLAT}	30	14.735
K_{ILAT}	10	16.441
K_{DLAT}	30	10.730
C_{LAT}	24.556	19.974

2.5.2. Flight Simulations

The longitudinal and lateral closed-loop control systems were simply constituted in the MATLAB/Simulink environment to perform flight simulations (i.e., time-response analysis) of obstacle avoidance scenarios and test the final trajectory tracking performance of WIGEWs. The simulations covered 5-degree pitch and roll attitudes, tracked separately for the fly-over and level-turn modes defined in the mission profile. As this was a conceptual study, the disturbing effects (e.g., gusts) in real flight conditions were not considered in the simulations.

To summarize the process, when the aircraft faces an obstacle, the obstacle detection sensors identify the distance between the aircraft and the obstacle, together with its size, and provide a decision as an input to the PID controllers, which are 5-degree pitch or

5-degree roll attitudes to be tracked. The controllers refer to the constructed dynamic models in terms of aileron or elevator deflections to obtain the corresponding attitude. The main objective of the control system is to track these trajectories with the fastest response and lowest error possible. In order to test the robustness of the base and optimized control systems, a time-response test was carried out, which comprised a flight simulation. The block diagram of the simulation process, including obstacle avoidance scenarios, is shown in Figure 17.

The results of the step-response analysis are presented in Figure 18 for both the base and optimized designs, to facilitate comparison. The fly-over mode simulations demonstrated a satisfactory improvement in settling time, of 69.96%, and in maximum overshoot, of 94.59%, together with a minor enhancement in rise time, of 13.27%. In level-turn simulations, the settling time was found to have worsened by 95.06% in contrast to the enhancements obtained in maximum overshoot, of 56.59%, and in rise time, of 27.17%. As a result, the final (i.e., optimized) design for WIGE-WS showed a satisfactory performance in both of the obstacle avoidance scenarios, as desired. The results of the simulations are summarized in terms of time-response parameters in comparison with the initial values, in Table 6.

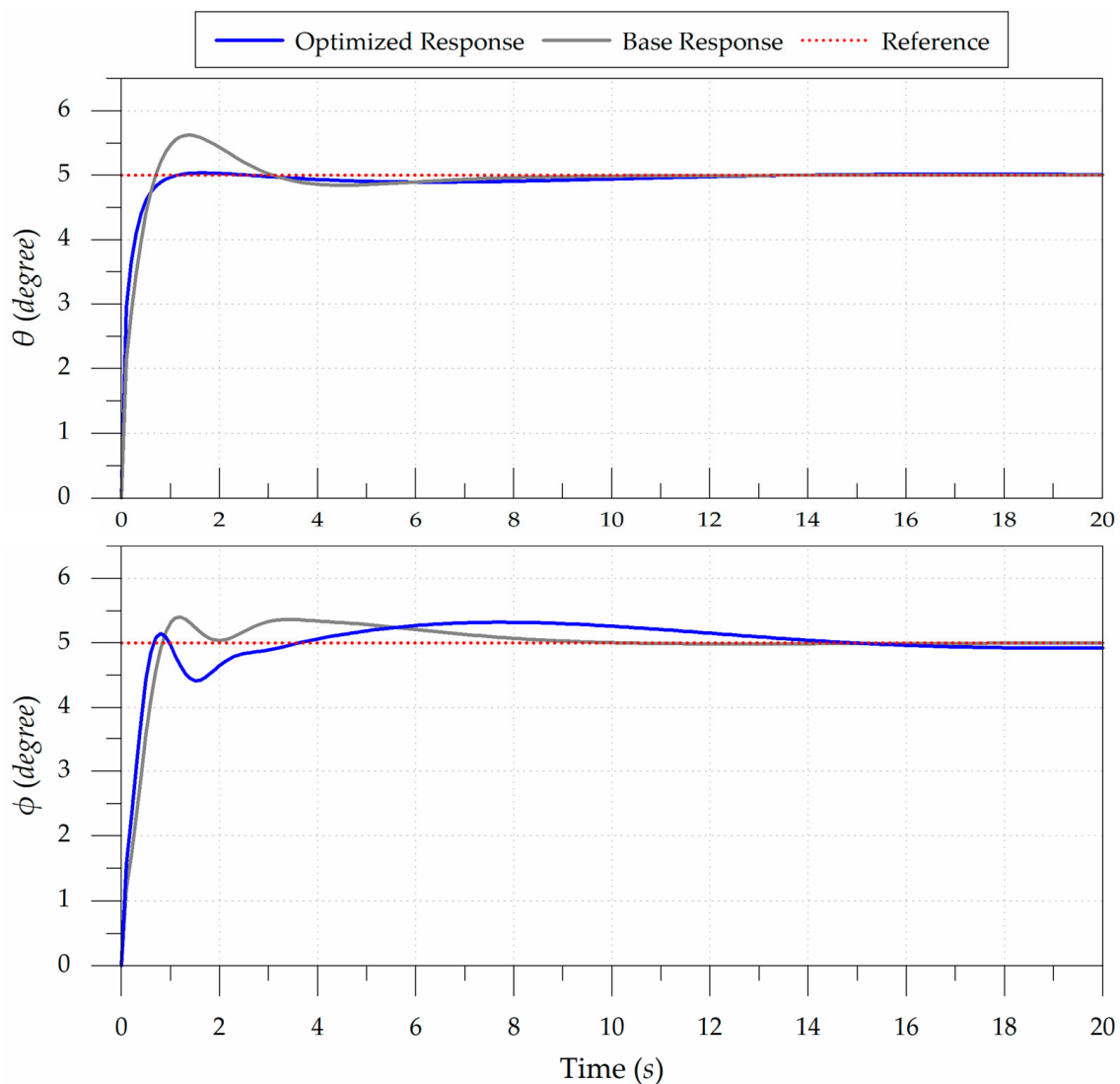


Figure 18. Longitudinal and lateral step responses of WIGE-WS AFCS.

3. Discussion and Conclusions

This paper introduces the conceptual design of a novel autonomous water sampling WIGE UAV conducted with an artificial neural network-integrated concurrent engineering approach, aiming for an improved obstacle avoidance performance. The design and discussion of a WIGE aircraft for a water sampling mission is presented here for the first time in the literature; therefore, this study offers remarkable technical insights, as well as providing a background and inspiration for future studies. Furthermore, the artificial intelligence-assisted multidisciplinary optimization methodology applied serves as an integrated product development tool and encourages innovative design perspectives.

The conceptual design process was conventionally initialized with the definition of the mission profile and design requirements. Based on the base objectives, the main wing was designed with a 2.1 m span and a high taper ratio and anhedral angle, to benefit ground-effect phenomena more effectively and to have a stabilizing and supporting structural element at the wingtips while floating on the water surface. A T-tail configuration was preferred, allowing the empennage to have a horizontal tail at a distance from the wake of the main wing and sea waves, owing to the low ground clearance of the vehicle. Similarly, the electric-powered propulsion system was located at the upper side of the fuselage, in order to be protected from the corrosive and adverse effects of the seawater. The weight estimations for internal and external components yielded a maximum take-off weight of 18.4 kg, while the flight performance investigations into the initial design exhibited an 87.81 km range with a 5 kg payload, which met the design requirements.

The autonomous control system design was tailored simultaneously with the initial aerodynamic design by means of an artificial neural network-integrated concurrent engineering approach. In this context, the stochastic optimization of the control system parameters and flight altitude of the aircraft exhibited an aerodynamic-performance enhancement and good trajectory-tracking performance for both the fly-over and level-turn obstacle avoidance modes. The aerodynamic-performance improvement referred to an enhanced range or payload at the same rate, which offered a 91.25 km range with a 5 kg payload or an 80 km range with a 5.71 kg payload. From the perspective of the trajectory-tracking performance parameters, the remarkable response enhancements obtained in terms of rise time and maximum overshoot reductions have been decisive in the high speed of the response in avoiding collisions. While the increment in the settling time of the level-turn mode response appears enormous, it is acceptable, as it was following a trajectory with negligible error that did not have any impact on the obstacle avoidance performance.

Consequently, the implementation of the concurrent design approach revealed the potential of this type of interdisciplinary coordination during the initial step of the aircraft design process. However, as the conceptual design phase relies on low-fidelity tools, more precise investigations should be conducted during the preliminary design phase, such as computational fluid dynamics (CFD) analyses, wind-tunnel experiments, or flight tests. In future flight simulations, the disturbances created by atmospheric air movements such as gusts or turbulences should be included. Moreover, the structural issues of this WIGE aircraft should be specifically considered, due to the combined influence of the forces and moments originating from hydrodynamics and aerodynamics, especially in the take-off and landing flight phases.

Funding: This research received no external funding.

Data Availability Statement: The original contributions presented in this study are included in the article. Further inquiries can be directed to the corresponding author.

Conflicts of Interest: The author declares no conflicts of interest.

References

1. Dehkordi, M.M.; Nodeh, Z.P.; Dehkordi, K.S.; Salmanvandi, H.; Khorjestan, R.R.; Ghaffarzadeh, M. Soil, air, and water pollution from mining and industrial activities: Sources of pollution, environmental impacts, and prevention and control methods. *Results Eng.* **2024**, *23*, 102729. [[CrossRef](#)]
2. Sharma, K.; Rajan, S.; Nayak, S.K. Water pollution: Primary sources and associated human health hazards with special emphasis on rural areas. In *Water Resources Management for Rural Development*; Elsevier: Amsterdam, The Netherlands, 2024; pp. 3–14.
3. Yu, X.; Wang, Y.; Watson, P.; Yang, X.; Liu, H. Application of passive sampling device for exploring the occurrence, distribution, and risk of pharmaceuticals and pesticides in surface water. *Sci. Total Environ.* **2024**, *908*, 168393. [[CrossRef](#)]
4. Kaizu, Y.; Iio, M.; Yamada, H.; Noguchi, N. Development of unmanned airboat for water-quality mapping. *Biosyst. Eng.* **2011**, *109*, 338–347. [[CrossRef](#)]
5. Leistenschneider, C.; Wu, F.; Primpke, S.; Gerdt, G.; Burkhardt-Holm, P. Unveiling high concentrations of small microplastics (11–500 μm) in surface water samples from the southern Weddell Sea off Antarctica. *Sci. Total Environ.* **2024**, *927*, 172124. [[CrossRef](#)]
6. Shil, S.; Singh, U.K.; Mehta, P. Water quality assessment of a tropical river using water quality index (WQI), multivariate statistical techniques and GIS. *Appl. Water Sci.* **2019**, *9*, 168. [[CrossRef](#)]
7. Judran, N.H.; Kumar, A. Evaluation of water quality of Al-Gharraf River using the water quality index (WQI). *Model. Earth Syst. Environ.* **2020**, *6*, 1581–1588. [[CrossRef](#)]
8. Mucciarone, D.A.; DeJong, H.B.; Dunbar, R.B.; Takeshita, Y.; Albright, R.; Mertz, K. Autonomous submersible multiport water sampler. *HardwareX* **2021**, *9*, e00197. [[CrossRef](#)] [[PubMed](#)]
9. Neumann, K.C.; La, D.; Yoo, H.; Burkepile, D.E. Programmable Autonomous Water Samplers (PAWS): An inexpensive, adaptable and robust submersible system for time-integrated water sampling in freshwater and marine ecosystems. *HardwareX* **2023**, *13*, e00392. [[CrossRef](#)]
10. Manoharan, D.; Gajendran, C.; Padmanabhan, M.K.; Vignesh, S.; Rajesh, S.; Bhuvaneshwaran, G.D. Design and development of autonomous amphibious unmanned aerial vehicle for in situ water quality assessment and water sampling. *J. Unmanned Veh. Syst.* **2021**, *9*, 182–204. [[CrossRef](#)]
11. Sanim, K.R.I.; Kalaitzakis, M.; Kosaraju, B.; Kitzhaber, Z.; English, C.; Vitzilaios, N.; Myrick, M.; Hodgson, M.; Richardson, T. Development of an aerial drone system for water analysis and sampling. In Proceedings of the International Conference on Unmanned Aircraft Systems (ICUAS), Dubrovnik, Croatia, 21–24 June 2022.
12. Ore, J.P.; Elbaum, S.; Burgin, A.; Detweiler, C. Autonomous aerial water sampling. *J. Field Robot.* **2015**, *32*, 1095–1113. [[CrossRef](#)]
13. Koparan, C.; Koc, A.B.; Privette, C.V.; Sawyer, C.B. Adaptive water sampling device for aerial robots. *Drones* **2020**, *4*, 5. [[CrossRef](#)]
14. Koparan, C.; Koc, A.B.; Privette, C.V.; Sawyer, C.B.; Sharp, J.L. Evaluation of a UAV-assisted autonomous water sampling. *Water* **2018**, *10*, 655. [[CrossRef](#)]
15. Román, A.; Tovar-Sánchez, A.; Gauci, A.; Deidun, A.; Caballero, I.; Colica, E.; D’Amico, S.; Navarro, G. Water-quality monitoring with a UAV-mounted multispectral camera in coastal waters. *Remote Sens.* **2023**, *15*, 237. [[CrossRef](#)]
16. Hagh, S.F.; Amngostar, P.; Zylka, A.; Zimmerman, M.; Cresanti, L.; Karins, S.; O’Neil-Dunne, J.P.; Ritz, K.; Williams, C.J.; Morales-Williams, A.M.; et al. Autonomous UAV-mounted LoRaWAN system for real-time monitoring of harmful algal blooms (HABs) and water quality. *IEEE Sens. J.* **2024**, *24*, 11414–11424. [[CrossRef](#)]
17. Neto, J.C.D.; Resque, I.S.; Avelino, R.A.; Dos Santos, V.B.; Leite, L.S.; Cesar, L.O.; Belo, P.H.S.; Albuquerque, J.; Filho, J.L.L. An adapted unmanned aerial vehicle for environmental water sampling. *Química Nova* **2022**, *45*, 734–741. [[CrossRef](#)]
18. English, C.M.; Kitzhaber, Z.B.; Sanim, K.R.I.; Kalaitzakis, M.; Kosaraju, B.; Pinckney, J.L.; Hodgson, M.E.; Vitzilaios, N.I.; Richardson, T.L.; Myrick, M.L. Chlorophyll fluorometer for intelligent water sampling by a small uncrewed aircraft system (sUAS). *Appl. Spectrosc.* **2023**, *77*, 94–105. [[CrossRef](#)] [[PubMed](#)]
19. Erjic, C.; Zhang, X. Ground effect aerodynamics. In *Encyclopedia of Aerospace Engineering*; John Wiley & Sons Ltd.: Hoboken, NJ, USA, 2010.
20. Raymond, A.E. *Ground Influence on Airfoils*; NACA Technical Note, No.67, Document ID: 19930080862; NASA: Washington, DC, USA, 1921.
21. Reid, E.G. *A Full-Scale Investigation of Ground Effect*; US Government Printing Office: Washington, DC, USA, 1927.
22. Yun, L.; Bliault, A.; Doo, J. Ground Effect Craft Technology. In *WIG Craft and Ekranoplan*; Springer: Boston, MA, USA, 2010.
23. Rozhdestvensky, K.V. Wing-in-ground effect vehicles. *Prog. Aerosp. Sci.* **2006**, *42*, 211–283. [[CrossRef](#)]
24. Halloran, M.; O’Meara, S. *Wing in Ground Effect Craft Review*; Sir Lawrence Wackett Centre for Aerospace Design Technology, Royal Melbourne Institute of Technology: Melbourne, Australia, 1999.
25. Hameed, H. The design of a four-seat reverse delta WIG craft. *Maldives Natl. J. Res.* **2019**, *7*, 7–28. [[CrossRef](#)]
26. Swidan, A.; Joiner, K.; Jewson, E.; Carroll, N.; Champ, D.; Shpak, G. A Novel flying and diving wig craft for electronics intelligence—A conceptual design. In Proceedings of the International Telecommunications Conference (ITC-Egypt), Alexandria, Egypt, 26–28 July 2022.
27. Papadopoulos, C.; Mitridis, D.; Yakinthos, K. Conceptual Design of a novel unmanned ground effect vehicle (UGEV) and flow control integration study. *Drones* **2022**, *6*, 25. [[CrossRef](#)]
28. Raymer, D.P. *Aircraft Design: A Conceptual Approach*, 6th ed.; American Institute of Aeronautics and Astronautics Inc.: Reston, VA, USA, 2018.

29. Zodiatis, G.; Galanis, G.; Nikolaidis, A.; Kalogeri, C.; Hayes, D.; Georgiou, G.C.; Chu, P.C.; Kallos, G. Wave energy potential in the eastern mediterranean levantine basin. An integrated 10-year study. *Renew. Energy* **2014**, *69*, 311–323. [[CrossRef](#)]
30. Barbariol, F.; Davison, S.; Falcieri, F.M.; Ferretti, R.; Ricchi, A.; Sclavo, M.; Benetazzo, A. Wind waves in the mediterranean sea: An ERA5 reanalysis wind-based climatology. *Front. Mar. Sci.* **2021**, *8*, 760614. [[CrossRef](#)]
31. International Maritime Organization Issued Guidelines for Wing-in-Ground Craft. Available online: <https://www.wcdn.imo.org/localresources/en/OurWork/Safety/Documents/MSC.1-CIRC.1592.pdf> (accessed on 9 November 2024).
32. Sadraey, M.H. *Design of Unmanned Aerial Systems*; John Wiley & Sons Ltd.: Hoboken, NJ, USA, 2020.
33. Nelson, R.C. *Flight Stability and Automatic Control*, 2nd ed.; WCB/McGraw-Hill: New York, NY, USA, 1998.
34. Yun, J.Y.; Hwang, H.Y. Technology identification, evaluation, selection, and optimization of a HALE solar aircraft. *Appl. Sci.* **2020**, *10*, 7593. [[CrossRef](#)]
35. Ahmad, M.; Hussain, Z.L.; Shah, S.I.A.; Shams, T.A. Estimation of stability parameters for wide body aircraft using computational techniques. *Appl. Sci.* **2021**, *11*, 2087. [[CrossRef](#)]
36. Jesudasan, R.; Hanifi, A.; Mariani, R. Investigating planar and nonplanar wing planform optimisation for ground effect aircraft. *Aerospace* **2023**, *10*, 969. [[CrossRef](#)]
37. Kim, H.J.; Chun, H.H.; Jung, K.H. Aeronumeric optimal design of a wing-in-ground-effect craft. *J. Mar. Sci. Technol.* **2009**, *14*, 39–50. [[CrossRef](#)]
38. Tofa, M.M.; Maimun, A.; Ahmed, Y.M.; Jamei, S.; Priyanto, A.; Rahimuddin. Experimental investigation of a wing-in-ground effect craft. *Sci. World J.* **2014**, *2014*, 89308. [[CrossRef](#)] [[PubMed](#)]
39. Güven, K.; Şamiloğlu, A.T. System identification of an aerial delivery system with a ram-air parachute using a NARX network. *Aerospace* **2022**, *9*, 443. [[CrossRef](#)]
40. Zhao, S.; Tao, X.; Li, Z. Initial identification of thrust and orbit elements for continuous thrust spacecraft in circular orbit. *Aerospace* **2023**, *10*, 1012. [[CrossRef](#)]
41. Amelin, K.; Maltsev, V. Using of the SPSA method to improve the accuracy of UAV following a given route under the action of wind loads. *Cybern. Phys.* **2021**, *10*, 224–230. [[CrossRef](#)]
42. Zhu, B.; Xu, S.; Rice, F.; Doğançay, K. Angle-of-arrival target tracking using a mobile UAV in external signal-denied environment. In Proceedings of the IEEE International Conference on Acoustics, Speech and Signal Processing (ICASSP), Rhodes Island, Greece, 4–10 June 2023.
43. Alahvirdi, D.; Tuci, E. Autonomous traffic monitoring and management by a simulated swarm of UAVs. In Proceedings of the 11th RSI International Conference on Robotics and Mechatronics (ICRoM), Tehran, Iran, 19–21 December 2023.
44. Sha, D.; Gao, J.; Yang, D.; Zuo, F.; Ozbay, K. Calibrating stochastic traffic simulation models for safety and operational measures based on vehicle conflict distributions obtained from aerial and traffic camera videos. *Accid. Anal. Prev.* **2023**, *179*, 106878. [[CrossRef](#)] [[PubMed](#)]
45. Wang, L.; Spall, J.C. Improved SPSA using complex variables with applications in optimal control problems. In Proceedings of the 2021 American Control Conference (ACC), New Orleans, LA, USA, 25–28 May 2021.
46. Kose, O. Stochastic optimal tuning for flight control system of morphing arm octorotor. *Aircr. Eng. Aerosp. Technol.* **2024**, *96*, 669–678. [[CrossRef](#)]
47. Spall, J. Multivariate stochastic approximation using a simultaneous perturbation gradient approximation. *IEEE Trans. Autom. Control* **1992**, *37*, 332–341. [[CrossRef](#)]
48. Sadegh, P.; Spall, J.C. Optimal random perturbation for stochastic approximation using a simultaneous perturbation gradient approximation. *IEEE Trans. Autom. Control* **1998**, *43*, 1480–1484. [[CrossRef](#)]

Disclaimer/Publisher’s Note: The statements, opinions and data contained in all publications are solely those of the individual author(s) and contributor(s) and not of MDPI and/or the editor(s). MDPI and/or the editor(s) disclaim responsibility for any injury to people or property resulting from any ideas, methods, instructions or products referred to in the content.